PHYSICAL REVIEW B **103**, 214104 (2021)

Polarization rotation by external electric field in the two-dimensional antiferroelectric squaric acid $H_2C_4O_4$

A. P. Moina*
Institute for Condensed Matter Physics, 1 Svientsitskii Street, 79011, Lviv, Ukraine

(Received 27 October 2020; revised 12 May 2021; accepted 12 May 2021; published 1 June 2021)

A pseudospin model for description of the influence of the electric field, confined to the plane of sublattice polarization, on the two-dimensional squaric acid antiferroelectrics is developed. The temperature–electric field T-E_1 phase diagram is constructed. Most of the field-induced transitions are found to be associated with polarization rotation. The system behavior is best characterized by the introduced noncollinearity angle θ, which is the angle between the sublattice polarizations. The collinear ferroelectric phase and two noncollinear phases with almost antiparallel and perpendicular polarizations of the sublattices are identified. The diagram also contains the crossover region, where the noncollinearity angle varies continuously between, nominally, 180° and 90°. The first- and second-order transition lines, supercritical lines, critical and two bicritical end points, and the tricritical point on the T-E_1 phase diagram are detected. Three plateaus are observed in the field dependence of the net polarization at low temperatures.

DOI: 10.1103/PhysRevB.103.214104

I. INTRODUCTION

The squaric acid $H_2C_4O_4$ (3,4-dihydroxy-3-cyclobutene-1,2-dione) is a classical example of a two-dimensional antiferroelectric. In these crystals, the hydrogen-bonded C_4O_4 groups form sheets parallel to the *ac* plane and stacked along the *b* axis. Below the transition at 373 K, a spontaneous polarization arises in these sheets, with the neighboring sheets polarized in the opposite directions [1–3]. At the transition, the crystal symmetry changes from centrosymmetric tetragonal, $I4/m$, to monoclinic, $P2_1/m$.

Protons on the hydrogen bonds in squaric acid move in double-well potentials, so each of the protons can occupy a site closer to the C_4O_4 group or the other site on the bond, closer to the neighboring C_4O_4 group. The C_4O_4 groups possess C_{1h} symmetry both below and above the transition [4]; the distortion from the square shape is caused by formation of a double bond between those two adjacent carbon atoms, closer to which two protons on the hydrogen bonds sit. The sublattice polarization is mostly electronic, while the direct contribution of ions and displaced protons is significantly smaller [5].

External electric fields produce many interesting effects in antiferroelectrics. Probably the best known is the switching of a negative sublattice polarization by the bias field and the resulting transition from the antiferroelectric (AFE) to a ferroelectric (FE) phase, manifesting itself in the classical double *P-E* hysteresis loops. Typical high permittivity and dielectric strength of antiferroelectrics as well as a small remnant polarization of the double loops make these systems promising candidates for use in the high-energy-storage capacitors.

In conventional ferroelectrics, the external electric field applied along the axis of spontaneous polarization is a field conjugate to the order parameter. The T-E phase diagram in the case of the first-order phase transition at zero field is simple. The transition temperature increases with the field, and the transition line ends at the critical point [6–9]. At the fields above the critical one, the rounded maxima of the dielectric permittivity are observed along the so-called Widom line [7–9]. In the case of antiferroelectrics, there is no physically realizable electric field conjugate to the sublattice polarization, and the phase diagram is much more complicated.

Okada *et al.* [10–12] and recently Tolèdano [13] explored the T-E phase diagram of a uniaxial antiferroelectric using the phenomenological approach. In particular, it has been found [10–12] that apart from the field-induced FE phase, there exists an additional semipolar phase at elevated fields, where an incomplete compensation of the sublattice polarizations occurs.

In contrast to the uniaxial antiferroelectrics, where the average sublattice polarization is either parallel or antiparallel to the predetermined direction, the pseudotetragonal symmetry of the squaric acid crystal lattice and, foremost, of its two-dimensional hydrogen bond networks, permits 90° rotations of the sublattice polarizations by the applied electric field. Hysteresis loop measurements and Berry phase calculations by Horiuchi *et al.* [5] have given evidence for such a rotation. Microscopically, it would invoke a relocation of one of the two protons in each molecule to the other site along the same hydrogen bond and a simultaneous switching of the π bond to those carbon atoms, close to which the protons would sit after the relocation. Further calculations [14] have shown that the field-induced sublattice polarization rotation by 90° is possible at different orientations of the field within the *ac* plane. It is also predicted [5,14] that higher fields, in particular $E_1 \pm E_3$ applied along the diagonals of the *ac* plane, can relocate the second proton of each molecule along the hydrogen bond, resulting in a 180° rotation of the negative

---

*alla@icmp.lviv.ua

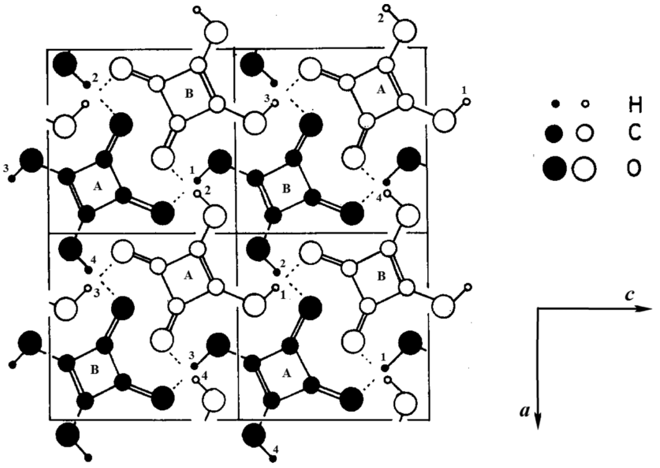

FIG. 1. Crystal structure of squaric acid as viewed along the *b* axis. Figure is taken from Refs. [19,20]. Two adjacent layers are shown, with black and open circles each. The A- and B-type C_4O_4 groups are indicated (see text for explanation), and the hydrogen bonds are numbered.

sublattice polarization as compared to the initial AFE phase and inducing the collinear ferroelectric phase, analogous to that in uniaxial antiferroelectrics.

Theoretical model description of the antiferroelectric transition in squaric acid is usually based on a certain version of the proton ordering model, invoking four-particle correlations between protons within the planes [15–18]. The four-particle Hamiltonians are basically identical to those for $NH_4H_2PO_4$ crystals, antiferroelectrics of the KH_2PO_4 family. Recently we have developed a deformable four-particle model for squaric acid [19] that describes the effects associated with the diagonal lattice strains and changes in the hydrogen bond geometry: the thermal expansion, influence of external hydrostatic pressure, and dependence of the interaction constants on the H-site distance δ.

In the present paper, we shall modify our recently proposed model [19] to take into account the changes in the system symmetry caused by the electric fields applied within the plane of the hydrogen bonds. The system Hamiltonian, thermodynamic potential, and equations for the order parameters and lattice strains are obtained in Sec. II. Results of numerical calculations are presented in Sec. III, where the temperature–electric field phase diagram is constructed. The Appendix contains a thorough coverage of the variety of the temperature dependences of the order parameters, strains, and static dielectric permittivity at different values of the field.

II. THE MODEL

There are two formula units in the low-temperature phase unit cell of squaric acid. In our model, the unit cell consists of two C_4O_4 groups and four hydrogen atoms ($f = 1, 2, 3, 4$; see Fig. 1) attached to one of them (the A-type group). All hydrogens around the B-type groups are considered to belong to the A-type groups, with which the B groups are hydrogen bonded. Note that the two C_4O_4 groups of each unit cell belong to different neighboring layers. The center of each hydrogen bond lies exactly above the center of the hydrogen bond in the layer below it (as seen along the *b* axis).

As usually in the proton ordering models, we consider interactions between protons, leading to ordering in their system. Motion of protons in double-well potentials is described by Ising pseudospins, whose two eigenvalues $\sigma_{yqf} = \pm 1$ are assigned to two equilibrium positions of the fth proton. Here y stands for the layer index, and q is the index of the A-type C_4O_4 group. It is assumed that the crystal is placed into electric fields E_1 and E_3 directed along the *a* and *c* axes.

The system Hamiltonian [19]

$$H = NU_{\text{seed}} + H^{\text{intra}}_{\text{long}} + H^{\text{inter}}_{\text{long}} + H_{\text{short}} \qquad (1)$$

includes ferroelectric intralayer long-range interactions $H^{\text{intra}}_{\text{long}}$, ensuring ferroelectric ordering within each separate layer, antiferroelectric interlayer interactions $H^{\text{inter}}_{\text{long}}$ responsible for alternation of polarizations in the stacked layers, and the short-range configurational interactions between protons H_{short}, which include also the interactions with external electric fields. Here N is the number of the unit cells in the crystal.

The so-called seed energy [19] in the Hamiltonian

$$U_{\text{seed}} = \frac{v}{2}\sum_{ij=1}^{3} c^{(0)}_{ij} u_i u_j - v\sum_{ij=1}^{3} c^{(0)}_{ij}\alpha^{(0)}_i \big(T - T^0_i\big) u_j \qquad (2)$$

corresponds to the deformable host lattice of heavy ions that forms the double-well potentials for the motion of protons. It contains elastic and thermal expansion contributions associated with uniform diagonal lattice strains u_1, u_2, and u_3; $c^{(0)}_{ij}$ and $\alpha^{(0)}_i$ are the seed elastic constants and thermal expansion coefficients; T^0_i determine the reference point of the thermal expansion of the crystal, which can be chosen arbitrarily; and v is the unit cell volume at this reference point. Contributions of the monoclinic strain u_5 are ignored. Note that for the indices of the second-rank tensors u and $\alpha^{(0)}$ and of the fourth-rank tensor $c^{(0)}$ the usual Voigt notations $11 \rightarrow 1$, $22 \rightarrow 2$, $33 \rightarrow 3$, $13 \rightarrow 5$ [21] are used throughout the paper. The Hooke's law for the thermally expanding host lattice, following from U_{seed}, allows us [19] to describe correctly the regular thermal expansion of squaric acid, observed in the paraelectric phase, as well as the hydrostatic pressure dependence of the lattice constants. The theoretical anomalous behavior of the strains below the antiferroelectric transition, caused by coupling of the host heavy ion lattice to the subsystem of ordered protons, is also in a very good agreement with experimental data [19].

The short-range Hamiltonian H_{short} describes the four-particle configurational correlations between protons sitting around each C_4O_4 group. It is assumed that the energy of four lateral configurations $\mathcal{E}_a$, where two protons are in positions close to the adjacent oxygens of the C_4O_4 group and two other protons are closer to the neighboring C_4O_4 groups (see Fig. 2 and Table I, configurations 1–4), is the lowest of all. This level is thus four times degenerate in the absence of an external electric field. The next level is two diagonal configurations with the energy $\mathcal{E}_s$, where the protons are close to the opposite oxygens of the C_4O_4 group (configurations 5 and 6 in Table I). Then there are eight single-ionized configurations with three or only one close protons, having the energy $\mathcal{E}_1$ (configurations 7–14), and two double-ionized configurations with four

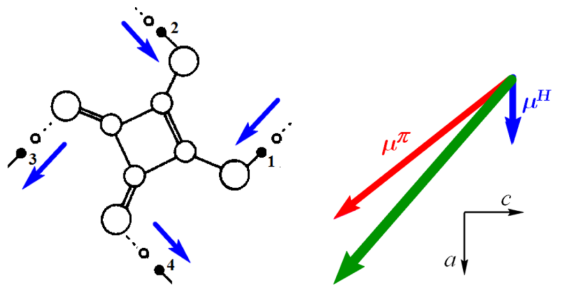

FIG. 2. Dipole moments of the lateral proton configuration (configuration 1 of Table I) around an A-type C_4O_4 group, as deduced from the results of Ref. [5]. $\boldsymbol{\mu}_1^H = (2\mu^H, 0, 0)$, $\boldsymbol{\mu}_1^\pi = (2\mu_\parallel^\pi, 0, -2\mu_\perp^\pi)$. Directions of the dipole moments associated with protons and with electrons are shown by blue and red arrows, respectively; the green arrow is the total dipole moment of the configuration; and the vector lengths are nominal.

or zero protons ($\mathcal{E}_0$, configurations 15 and 16). We accept that $\mathcal{E}_a < \mathcal{E}_s \ll \mathcal{E}_1 \ll \mathcal{E}_0$. Lateral proton configurations, being the ground-state ones in squaric acid, are confirmed by structural measurements (e.g., Refs. [1,5]).

The electric fields E_1 and E_3 remove the degeneracy of the lowest level of four lateral proton configurations $\mathcal{E}_a$, as well as of the second excited level of single-ionized configurations $\mathcal{E}_1$. The energies of the diagonal (5 and 6) and double-ionized (15 and 16) proton configurations, having no dipole moment in the *ac* plane, remain unchanged.

Our modeling of the electric field influence on the squaric acid is heavily based on the results of the Berry phase calculations [5], which have shown that the sublattice polarization in this crystal is formed predominantly by the electronic contributions of switchable π-bond dipoles, rather than directly by displacements of protons along the hydrogen bonds. Positions of the double bonds, however, are determined by the proton configurations around the given C_4O_4 group: In the ground-state lateral configurations, the bond is formed between the two neighboring carbons, near which protons sit on the hydrogen bonds (see Fig. 2), and also between the carbons and adjacent to them oxygens, next to which there is no proton (meaning that the protons on these bonds sit in the minima close to the neighboring C_4O_4 groups).

Directions of the electronic and total sublattice polarizations are, at least at low temperatures, determined by populations of the four ground-state lateral proton configurations in the sublattice. For the configuration 1, these directions are depicted in Fig. 2. The proton contribution vector goes along the [100] axis, while the electronic contribution is at an angle to it. The three other lateral configurations and their dipole moments can be obtained from the scheme of Fig. 2 by rotation by a multiple of 90°. It is taken that in absence of the electric field the protons in the AFE phase are mostly in configuration 1 in the positively polarized sublattice and in configuration 3 in the negatively polarized sublattice. Then, the observed [5] 90° switching of polarization means that the protons in the negatively polarized sublattice move from the configuration 3 to configuration 2 or 4, and the total 180° rotation of polarization means switching to configuration 1.

No polarization calculations for the single-ionized configurations, like the Berry phase calculations for the lateral

TABLE I. Proton configurations and their energies $\widetilde{\mathcal{E}}_i$ in presence of the electric fields E_1 and E_3; $W_3 = \mu^H E_1 + \mu_\parallel^\pi E_1 - \mu_\perp^\pi E_3$; $W_1 = -\mu^H E_3 - \mu_\parallel^\pi E_3 - \mu_\perp^\pi E_1$. Directions of the dipole moments associated with protons and with electrons are shown by blue and green arrows, respectively.

i	$s_1s_2s_3s_4$		$\widetilde{\mathcal{E}}_i$
1	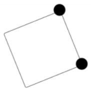 $++--$		$\mathcal{E}_a - 2W_3$
2	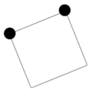 $-++-$		$\mathcal{E}_a + 2W_1$
3	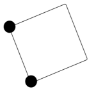 $--++$		$\mathcal{E}_a + 2W_3$
4	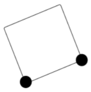 $+--+$		$\mathcal{E}_a - 2W_1$
5	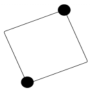 $-+-+$		$\mathcal{E}_s$
6	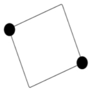 $+-+-$		$\mathcal{E}_s$
7	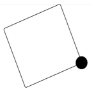 $+---$	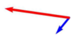	$\mathcal{E}_1 - W_1 - W_3$
8	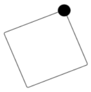 $-+--$		$\mathcal{E}_1 + W_1 - W_3$
9	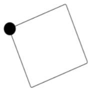 $--+-$	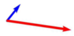	$\mathcal{E}_1 + W_1 + W_3$
10	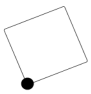 $---+$		$\mathcal{E}_1 - W_1 + W_3$
11	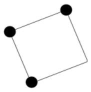 $-+++$	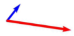	$\mathcal{E}_1 + W_1 + W_3$
12	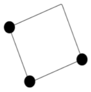 $+-++$		$\mathcal{E}_1 - W_1 + W_3$
13	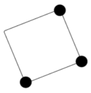 $++-+$		$\mathcal{E}_1 - W_1 - W_3$
14	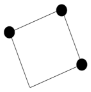 $+++-$		$\mathcal{E}_1 + W_1 - W_3$
15	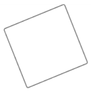 $----$		$\mathcal{E}_0$
16	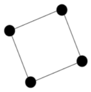 $++++$		$\mathcal{E}_0$

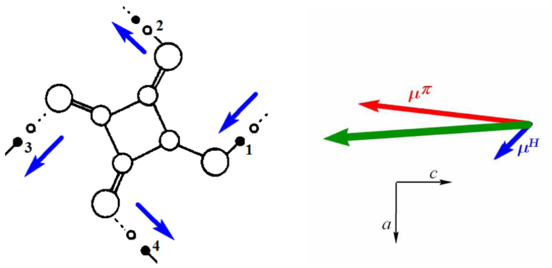

FIG. 3. Dipole moments of the single-ionized proton configuration with one proton (configuration 7 of Table I). $\boldsymbol{\mu}_7^H = (\mu^H, 0, -\mu^H)$, $\boldsymbol{\mu}_7^\pi = (\mu_\parallel^\pi - \mu_\perp^\pi, 0, -\mu_\parallel^\pi - \mu_\perp^\pi)$.

configurations [5], has been performed yet. Hence, while the direction of the protonic polarization can be easily determined, the direction of the electronic polarization for them is largely a guesswork. As one can see in Fig. 2, for the lateral configurations the electronic dipole moment is directed, roughly, from the two protons toward the two double bonds between carbons and oxygens, next to which there is no proton, i.e., qualitatively, from the region of the lowest electron density to the region with the highest electron density. In analogy to the case of the lateral configurations, we shall assume that in the single-ionized configuration (Fig. 3), the electronic dipole moment is directed from the single proton toward the double bond between the oxygen and carbon along the diagonal of the C_4O_4 group. With the proton dipole moment directed at 45° to the crystallographic axes, we again obtain approximately the same angle between the the protonic and electronic polarization vectors, as in the case of the lateral configurations, and we shall assume that this angle is exactly the same.

Likewise, we assume that the ratio of the absolute values of the proton and electronic dipole moments is the same in lateral and in single-ionized configurations. For the lateral configurations, the absolute value of the proton dipole moment is denoted as $2\mu^H$. The electronic dipole moment vector has two components: $2\mu_\parallel^\pi$ along the direction of the proton dipole moment and $2\mu_\perp^\pi$ in the perpendicular direction. So, if we have $\boldsymbol{\mu}_1^H = (2\mu^H, 0, 0)$, $\boldsymbol{\mu}_1^\pi = (2\mu_\parallel^\pi, 0, -2\mu_\perp^\pi)$ for configuration 1 and $\boldsymbol{\mu}_7^H = (\mu^H, 0, -\mu^H)$ for configuration 7, then from the above assumptions it follows that $\boldsymbol{\mu}_7^\pi = (\mu_\parallel^\pi - \mu_\perp^\pi, 0, -\mu_\parallel^\pi - \mu_\perp^\pi)$.

For single-ionized configurations 11–14 with three protons, we use the same reasoning as above for configurations 7–10 with a single proton. In particular, the dipole moments of configuration 13 are the same as those of configuration 7. The dipole moments of all single-ionized configurations can be obtained by rotation of the the dipole moments of configurations 7 and 13. The dipole moment vectors and energies $\widetilde{\mathcal{E}}_i$ of all configurations in presence of the electric fields E_1 and E_3 are summarized in Table I.

In fact, exact orientation and magnitude of the electronic dipole moments of the single-ionized configurations are not too significant. These configurations represent the second excited energy level of the short-range part of the total Hamiltonian (1), lying at $(\mathcal{E}_1 - \mathcal{E}_a)/k_B = 1100\,\mathrm{K}$ [19] above the ground-state level. The magnitude of its splitting by the electric field is determined by the vector of the total dipole moment of these configurations (Fig. 3), only the electronic component of which has been guessed. Even though the actual electronic dipole moment most likely somewhat deviates from the guessed one, the error in the fraction of the correction to the energy of the second excited level of part of the total Hamiltonian, brought in by this deviation, is not expected to perceptibly affect the overall system behavior.

To go from the representation of proton configuration energies to the pseudospin representation, we use the standard procedure [19,22,23], according to which the Hamiltonian of the short-range correlations between protons surrounding each A-type C_4O_4 group is written as

$$H_{yq}^A = \sum_{i=1}^{16} \hat{N}_i(yq)\widetilde{\mathcal{E}}_i, \quad \hat{N}_i(yq) = \prod_{f=1}^{4} \frac{1}{2}(1 + s_f \sigma_{yqf}), \tag{3}$$

where $\hat{N}_i(yq)$ is the operator of the ith configuration, and $\widetilde{\mathcal{E}}_i$ is its energy. $s_f = \pm 1$ is the sign of the eigenvalue of the pseudospin σ_{yqf} operator in this particular configuration. It is assumed that $s_f = +1$ if the proton at the fth bond is localized at the H-site proximal to the given A-type C_4O_4 group, and $s_f = -1$ if the proton is localized at the other (distal) H site of the same bond. Using Eq. (3) and the energies $\widetilde{\mathcal{E}}_i$ given in Table I, we arrive at the following expression for the short-range Hamiltonian, identical to that used in the proton ordering model for the $NH_4H_2PO_4$-type antiferroelectrics (see, e.g., Ref. [24]):

$$\begin{aligned} H_{yq}^A = {} & V\left[\frac{\sigma_{yq1}}{2}\frac{\sigma_{yq2}}{2} + \frac{\sigma_{yq2}}{2}\frac{\sigma_{yq3}}{2} + \frac{\sigma_{yq3}}{2}\frac{\sigma_{yq4}}{2} + \frac{\sigma_{yq4}}{2}\frac{\sigma_{yq1}}{2}\right] \\ & + U\left[\frac{\sigma_{yq1}}{2}\frac{\sigma_{yq3}}{2} + \frac{\sigma_{yq2}}{2}\frac{\sigma_{yq4}}{2}\right] + \Phi\frac{\sigma_{yq1}}{2}\frac{\sigma_{yq2}}{2}\frac{\sigma_{yq3}}{2}\frac{\sigma_{yq4}}{2} \\ & - \sum_{f=1}^{4}[\mu_{f1}E_1 + \mu_{f3}E_3]\frac{\sigma_{yqf}}{2}. \end{aligned} \tag{4}$$

Here the short-range interaction constants

$$V = -\frac{\varepsilon - w_1}{2}, \quad U = \frac{\varepsilon + w_1}{2}, \quad \Phi = 2\varepsilon - 8w + 2w_1 \tag{5}$$

are linear functions of the Slater-Takagi type energy parameters

$$\varepsilon = \mathcal{E}_s - \mathcal{E}_a, \quad w = \mathcal{E}_1 - \mathcal{E}_a, \quad w_1 = \mathcal{E}_0 - \mathcal{E}_a.$$

It will be assumed that $w_1 \to \infty$. Finally, the dipole moments μ_{f1} and μ_{f3} are the following:

$$\begin{aligned} \mu_{11} &= -\mu_{31} = \mu^H + \mu_\parallel^\pi - \mu_\perp^\pi, \\ \mu_{21} &= -\mu_{41} = \mu^H + \mu_\parallel^\pi + \mu_\perp^\pi, \end{aligned} \tag{6}$$

and

$$\begin{aligned} \mu_{13} &= -\mu_{33} = -\mu^H - \mu_\parallel^\pi - \mu_\perp^\pi, \\ \mu_{23} &= -\mu_{43} = \mu^H + \mu_\parallel^\pi - \mu_\perp^\pi. \end{aligned} \tag{7}$$

It can be shown that just like for the KH_2PO_4 family crystals the contributions of the correlations of the protons around the A- and B-type groups to the total thermodynamic potential are equal. The Hamiltonian of the short-range interactions then can be written as

$$H_{\text{short}} \to 2\sum_{qy} H^{A}_{qy}, \tag{8}$$

where the expression for H^{A}_{qy} is given by Eq. (4).

The long-range interactions in the system Hamiltonian (1) are the dipole-dipole interactions, in analogy to the case of $\mathrm{KH_2PO_4}$ [22], renormalized by the proton-lattice coupling. The mean field approximation (MFA) is usually used for these interactions. In this approximation, we obtain the following expressions [19] for the long-range intralayer

$$\begin{aligned} H^{\text{intra}}_{\text{long}} &= -\frac{1}{2}\sum_{y=1}^{N_y}\sum_{\substack{qq'\\ ff'}} J^{\text{intra}}_{ff'}(qq')\frac{\sigma_{yqf}}{2}\frac{\sigma_{yq'f'}}{2} \\ &\simeq -2\sum_{yqf} F^{\text{intra}}_{yqf}\frac{\sigma_{yqf}}{2} + \sum_{yqf} F^{\text{intra}}_{yqf}\frac{\langle\sigma_{yqf}\rangle}{2}. \end{aligned} \tag{9}$$

and interlayer

$$\begin{aligned} H^{\text{inter}}_{\text{long}} &= -\frac{1}{2}\sum_{y}\sum_{y'\neq y}\sum_{\substack{qq'\\ ff'}} J^{\text{inter}}_{ff'}(yy';qq')\frac{\sigma_{yqf}}{2}\frac{\sigma_{y'q'f'}}{2} \\ &\simeq -2\sum_{yqf} F^{\text{inter}}_{yqf}\frac{\sigma_{yqf}}{2} + \sum_{yqf} F^{\text{inter}}_{yqf}\frac{\langle\sigma_{yqf}\rangle}{2} \end{aligned} \tag{10}$$

interactions. Here N_y is the total number of the layers. The internal mean fields are

$$\begin{aligned} F^{\text{intra}}_{yqf} &= \frac{1}{4}\sum_{q'f'} J^{\text{intra}}_{ff'}(qq')\langle\sigma_{yq'f'}\rangle, \\ F^{\text{inter}}_{yqf} &= \frac{1}{4}\sum_{y'q'f'} J^{\text{intra}}_{ff'}(yy;qq')\langle\sigma_{y'q'f'}\rangle. \end{aligned} \tag{11}$$

The four-particle cluster approximation will be used for the short-range interactions, described by the Hamiltonian (4). The thermodynamic potential of the system can be written as [19]

$$\begin{aligned} G = NU_{\text{seed}} &+ \sum_{yqf}\left(F^{\text{intra}}_{yqf} + F^{\text{inter}}_{yqf}\right)\frac{\langle\sigma_{yqf}\rangle}{2} - \frac{1}{\beta} \\ &\times\sum_{qy}\left[2\ln \mathrm{Sp}\exp\left(-\beta H^{(4)}_{qy}\right) - \sum_{f=1}^{4}\ln \mathrm{Sp}\exp\left(-\beta H^{(1)}_{qyf}\right)\right], \end{aligned} \tag{12}$$

where $\beta = (k_{\mathrm{B}}T)^{-1}$. The cluster Hamiltonian is

$$H^{(4)}_{qy} = H^{A}_{qy} - \sum_{f=1}^{4}\frac{z_{yqf}}{\beta}\frac{\sigma_{yqf}}{2}, \tag{13}$$

where

$$z_{yqf} = \beta\left[\Delta_{yqf} + 2F^{\text{intra}}_{yqf} + 2F^{\text{inter}}_{yqf} + \mu_{f1}E_1 + \mu_{f3}E_3\right].$$

The fields Δ_{yqf} are the effective cluster fields that describe short-range interactions of the spin σ_{yqf} with the particles from outside the cluster q. They are determined from the self-consistency condition, stating that the pseudospin mean values calculated with the four-particle (13) and with the one-particle

$$H^{(1)}_{yqf} = -[\Delta_{yqf} + z_{yqf}]\frac{\sigma_{yqf}}{2}$$

Hamiltonians must coincide.

The following symmetry of the pseudospin mean values was assumed for the antiferroelectrically ordered two-sublattice model in absence of external electric field [19]:

$$\langle\sigma_{yqf}\rangle = \exp[i\mathbf{k}_2\mathbf{R}_y]\eta_f. \tag{14}$$

Here $\mathbf{k}_2 = (0, b_2, 0)$; b_2 is the basis vector of the reciprocal lattice; the factor $\exp[i\mathbf{k}_2\mathbf{R}_y] = \pm 1$ denotes two sublattices of an antiferroelectric; and $\mathbf{R}_y$ is the position vector of the yth layer. We shall call the two sublattices of the model, where $\exp[i\mathbf{k}_2\mathbf{R}_y] = 1$ and -1, as the plus and minus sublattices, respectively. Neglecting the experimentally observed [1] weak nonequivalence of the hydrogen bonds linking the $\mathrm{C_4O_4}$ groups along the a and c axes, we described the system behavior in the absence of the field by the single order parameter η:

$$\eta \equiv \eta_1 = \eta_2 = -\eta_3 = -\eta_4. \tag{15}$$

In the presence of external electric fields E_1 or E_3, the mentioned nonequivalence can no longer be ignored. Also, the pseudospin mean values in the plus and minus sublattices differ not only by their signs, as in Eq. (14), but also by their absolute values. This leaves us with four independent order parameters,

$$\langle\sigma_{yqf}\rangle = \eta_{f\pm},$$

two for the plus and two for the minus sublattices,

$$\eta_{1\pm} = -\eta_{3\pm}; \quad \eta_{2\pm} = -\eta_{4\pm}, \tag{16}$$

in accordance with the system translational symmetry.

Taking into account Eq. (16), we can write the MFA Hamiltonians of the long-range interactions (9) and (10) as

$$\begin{aligned} H^{\text{intra}}_{\text{long}} + H^{\text{inter}}_{\text{long}} = N&\left[\nu\frac{(\eta_{1+}-\eta_{1-})^2}{4} + \nu\frac{(\eta_{2+}-\eta_{2-})^2}{4} + \nu'\frac{(\eta_{1+}+\eta_{1-})^2}{4} + \nu'\frac{(\eta_{2+}+\eta_{2-})^2}{4}\right] \\ &- 2\sum_{yq}\left[\frac{\sigma_{qy1}-\sigma_{qy3}}{2}\left(\nu\frac{\eta_{1+}-\eta_{1-}}{2} + \nu'\frac{\eta_{1+}+\eta_{1-}}{2}\right) + \frac{\sigma_{qy2}-\sigma_{qy4}}{2}\left(\nu\frac{\eta_{2+}-\eta_{2-}}{2} + \nu'\frac{\eta_{2+}+\eta_{2-}}{2}\right)\right]. \end{aligned} \tag{17}$$

The resulting interaction constants ν and ν' are linear combinations of the eigenvalues

$$\nu = \frac{J_{11}^{\text{intra}}(0) - J_{13}^{\text{intra}}(0)}{4} + \frac{J_{11}^{\text{inter}}(\mathbf{k}_2) - J_{13}^{\text{inter}}(\mathbf{k}_2)}{4},$$

$$\nu' = \frac{J_{11}^{\text{intra}}(0) - J_{13}^{\text{intra}}(0)}{4} + \frac{J_{11}^{\text{inter}}(0) - J_{13}^{\text{inter}}(0)}{4}, \qquad (18)$$

of the matrices of the long-range interaction constant Fourier transforms at the center of the Brillouin zone and at $\mathbf{k}_2$:

$$J_{ff'}^{\text{intra}}(0) = \sum_{q'} J_{ff'}^{\text{intra}}(qq'),$$

$$J_{ff'}^{\text{inter}}(0) = \sum_{q-q'}\sum_{y-y'} J_{ff'}^{\text{inter}}(yy';qq'),$$

$$J_{ff'}^{\text{inter}}(\mathbf{k}_2) = \sum_{q-q'}\sum_{y-y'} J_{ff'}^{\text{inter}}(yy';qq')\exp[i\mathbf{k}_2(\mathbf{R}_y - \mathbf{R}_{y'})]. \qquad (19)$$

We also took into account the the symmetry of the Fourier transforms over the bond indices f and f': $J_{11} = J_{22} = J_{33} = J_{44}, J_{12} = J_{23} = J_{34} = J_{41}, J_{13} = J_{24}$.

Eventually, the thermodynamic potential per one unit cell is obtained in the following form:

$$\frac{G}{N} = U_{\text{seed}} - \frac{1}{\beta}[\ln D_+ + \ln D_-] - \frac{1}{2\beta}\left[\ln\left(1-\eta_{1+}^2\right) + \ln\left(1-\eta_{2+}^2\right) + \ln\left(1-\eta_{1-}^2\right) + \ln\left(1-\eta_{2-}^2\right)\right]$$
$$+ \nu\frac{(\eta_{1+}-\eta_{1-})^2}{4} + \nu\frac{(\eta_{2+}-\eta_{2-})^2}{4} + \nu'\frac{(\eta_{1+}+\eta_{1-})^2}{4} + \nu'\frac{(\eta_{2+}+\eta_{2-})^2}{4}, \qquad (20)$$

where

$$D_\pm = a + \cosh(z_{1\pm} + z_{2\pm}) + 2b(\cosh z_{1\pm} + \cosh z_{2\pm}) + \cosh(z_{1\pm} - z_{2\pm}),$$
$$z_{f\pm} = \frac{1}{2}\ln\frac{1+\eta_{f\pm}}{1-\eta_{f\pm}} \pm \beta\nu\frac{\eta_{f+}-\eta_{f-}}{2} + \beta\nu'\frac{\eta_{f+}+\eta_{f-}}{2} + \beta\frac{\mu_{f1}E_1}{2} + \beta\frac{\mu_{f3}E_3}{2};$$
$$a = \exp(-\beta\varepsilon), \quad b = \exp(-\beta w).$$

The short-range Slater-Takagi energies, according to the model [19], are considered to be quadratic functions of the H-site distance δ. In its turn, the distance δ is taken to vary according to its experimentally observed [1] above the transition linear temperature dependence

$$\delta = \delta_0[1 + \delta_T(T - T_{\text{N0}})], \qquad (21)$$

where T_{N0} is the transition temperature at zero electric field. It yields

$$\varepsilon = \varepsilon_0'[1 + \delta_T(T - T_{\text{N0}})]^2, \quad w = w_0[1 + \delta_T(T - T_{\text{N0}})]^2. \qquad (22)$$

For the parameters of the long-range (dipole-dipole) interactions ν and ν', both the dependence of the dipole moments on δ and the variation of the interactions with the changes in the equilibrium distances between protons (dipoles) are taken into account [19]:

$$\nu = \nu_0[1 + \delta_T(T - T_{\text{N0}})]^2 + \sum_{i=1}^{3}\psi_i u_i,$$

$$\nu' = \nu_0'[1 + \delta_T(T - T_{\text{N0}})]^2 + \sum_{i=1}^{3}\psi_i' u_i. \qquad (23)$$

It should be mentioned that this form of the proton-lattice coupling can be obtained from a microscopic proton-phonon Hamiltonian by separating the uniform lattice strains in the atomic displacements (see, e.g., Ref. [25]).

Minimization of the thermodynamic potential (20) with respect to the order parameters $\eta_{f\pm}$ ($f = 1, 2$) and strains u_i yields the following equations:

$$\eta_{f\pm} = \frac{m_{f\pm}}{D_\pm}, \qquad (24)$$

$$0 = \sum_{j=1}^{3} c_{ij}^{(0)}\left[u_j - \alpha_j^{(0)}\left(T - T_j^0\right)\right]$$
$$+ \sum_{f=1}^{2}\left\{\psi_i\frac{\eta_{f+}-\eta_{f-}}{2v}\left[\frac{\eta_{f+}}{2} - \frac{\eta_{f-}}{2} - \frac{m_{f+}}{D_+} + \frac{m_{f-}}{D_-}\right]\right.$$
$$\left. + \psi_i'\frac{\eta_{f+}+\eta_{f-}}{2v}\left[\frac{\eta_{f+}}{2} + \frac{\eta_{f-}}{2} - \frac{m_{f+}}{D_+} - \frac{m_{f-}}{D_-}\right]\right\}, \qquad (25)$$

where

$$m_{f\pm} = \sinh(z_{1\pm} + z_{2\pm}) + 2b\sinh z_{f\pm} \pm \sinh(z_{1\pm} - z_{2\pm}).$$

The first sum in Eq. (25) describes the regular linear thermal expansion of a crystal, attributed entirely to the host lattice. The anomalous parts of the strains [the second sum in (25)], caused by the proton-lattice coupling, are quadratic functions of the order parameters $\eta_{f\pm}$, indicating the electrostrictive origin of these parts.

The net crystal polarizations P_1 and P_3 are

$$P_j = -\frac{1}{vN}\frac{\partial G}{\partial E_j} = P_{j+} + P_{j-}, \qquad (26)$$

where

$$P_{1\pm} = \frac{\mu^H + \mu_\parallel^\pi}{2v}(\eta_{1\pm} + \eta_{2\pm}) + \frac{\mu_\perp^\pi}{2v}(\eta_{2\pm} - \eta_{1\pm}),$$
$$P_{3\pm} = \frac{\mu^H + \mu_\parallel^\pi}{2v}(\eta_{2\pm} - \eta_{1\pm}) - \frac{\mu_\perp^\pi}{2v}(\eta_{2\pm} + \eta_{1\pm}) \quad (27)$$

are the sublattice polarizations. The total net polarization within the *ac* plane is

$$P = \sqrt{(P_{1+} + P_{1-})^2 + (P_{3+} + P_{3-})^2}. \quad (28)$$

The static dielectric permittivity ε_{11} can be found by numerical differentiation of the net polarization P_1 (26) with respect to the electric field E_1,

$$\varepsilon_{11} = \frac{1}{\varepsilon_0}\left(\frac{\partial P_1}{\partial E_1}\right)_p,$$

where $\varepsilon_0 \approx 8.85$ F/m is the electric constant. The differentiation is carried out at constant external pressures (stresses), equal to zero in our case, i.e., the permittivity of a mechanically free crystal is calculated.

III. CALCULATIONS

A. Fitting procedure

Even though the model developed here allows us to explore the influence of the electric field of any arbitrary orientation within the *ac* plane, we restrict our numerical calculations by the positive field E_1 only.

The thermodynamic potential is minimized numerically with respect to the order parameters $\eta_{f\pm}$. Simultaneously, the strains u_i are determined from Eqs. (25).

The values of most of the model parameters have been determined earlier [19]. They were required to provide the best fit to the experimental temperature curves of the sublattice polarization (order parameter) at ambient pressure, the temperature and hydrostatic pressure dependences of the lattice strains u_i, and the pressure dependence of the transition temperature T_N. Details of the fitting procedure are given in Ref. [19].

New to the present model are the parameters ν_0', ψ_i' [see Eq. (23)] and the dipole moments $\mu^H + \mu_\parallel^\pi$ and $\mu_\perp^\pi$. As discussed in the Appendix, the values of ψ_i', along with ψ_i, determine the behavior of the lattice strains at the field-induced phase transitions. No experimental data for this are available yet. For the sake of simplicity, we take for now that $\psi_i' = \psi_i$.

The parameter ν_0' and the dipole moments are determined by fitting the calculated curve of the dielectric permittivity ε_{11} at zero external bias field to the experimental points of Ref. [5], also considering the positions of the field-induced transitions predicted by the model. It is also required that $\mu^H + \mu_\parallel^\pi > \mu_\perp^\pi$, in accordance with the Berry phase calculations [5]. It cannot be said, however, that the adopted set of ν_0' and μ is unique. The ramifications of this uncertainty are discussed in more detail in Subsec. III C.

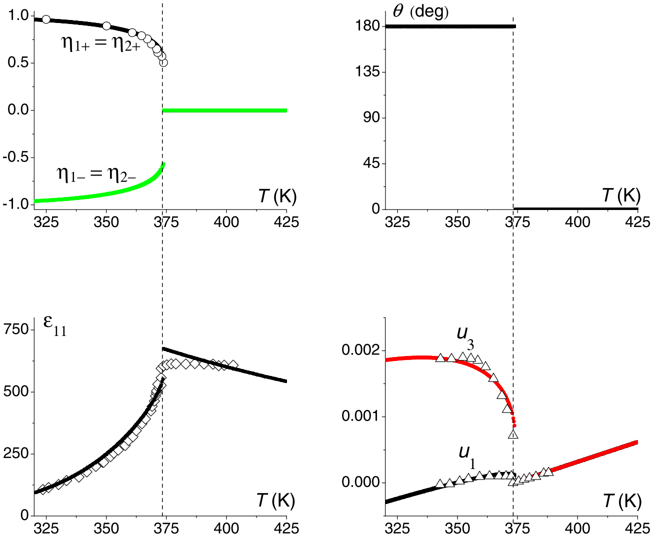

FIG. 4. The temperature dependences of the order parameters $\eta_{f\pm}$ (upper left), noncollinearity angle θ (upper right), dielectric permittivity ε_{11} (lower left), and lattice strains u_1 and u_3 (lower right) of squaric acid at $E_1 = 0$. Open symbols: experimental points, taken from Refs. [26] (○), [5] (◇), and [27] (△). Vertical dashed lines are a guide to the eye, showing the phase transition. The noncollinearity angle θ is introduced in Subsec. III B.

The obtained agreement with the experimental data in the absence of the electric field is illustrated in Fig. 4. The used values of the model parameters are given in Table II.

B. Polarization rotation and noncollinearity angle

To describe the process of polarization rotation by external electric fields, it is convenient to introduce a new parameter, the noncollinearity angle θ, i.e., the angle between polarization vectors of the plus and minus sublattices,

$$\theta = \left| \arccos\frac{\eta_{1+} + \eta_{2+}}{\sqrt{2\left(\eta_{1+}^2 + \eta_{2+}^2\right)}} - \arccos\frac{\eta_{1-} + \eta_{2-}}{\sqrt{2\left(\eta_{1-}^2 + \eta_{2-}^2\right)}} \right|. \quad (29)$$

The first and second terms here are the angles between the actual plus and minus sublattice polarization vectors

$$\mathbf{P}_\pm = (P_{1\pm}, 0, P_{3\pm}), \quad (30)$$

TABLE II. The adopted values of the model parameters. All, except μ and ν_0', are taken from Ref. [19].

ε_0'/k_B	w_0/k_B	ν_0/k_B	ν_0'/k_B (K)	ψ_1/k_B	ψ_2/k_B	ψ_3/k_B	c_{11}^0	c_{12}^0	c_{13}^0 (10^{10} N/m^2)	c_{22}^0	α_1^0	α_2^0 (10^{-5} K^{-1})	δ_T	v (10^{-28} m^3)	$\mu^H + \mu_\parallel^\pi$ (10^{-29} C m)	$\mu_\perp^\pi$
395	1100	79.9	−50	−518	445	1096	6.5	2.3	−3.1	2.38–0.02T	1.2	13.0	20	2.0	3.64	1.65

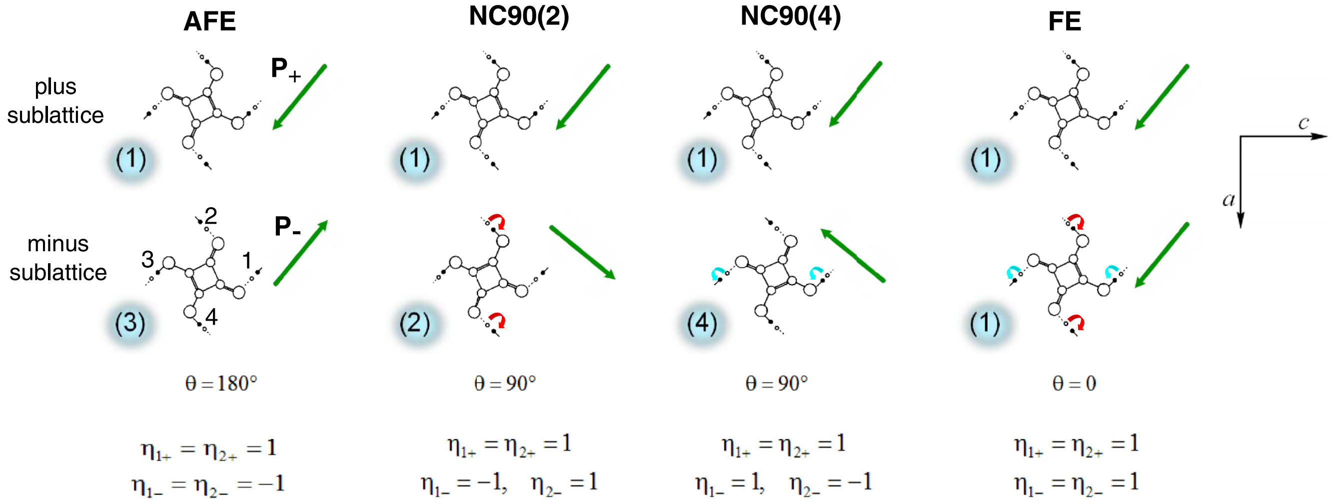

FIG. 5. The ground-state proton configurations, respective polarization vectors $\mathbf{P}_+$ and $\mathbf{P}_-$ of the plus and minus sublattices, the noncollinearity angle θ [the angle between the sublattice polarizations, Eq. (29)], and the values of the order parameters $\eta_{f\pm}$ at saturation for the antiferroelectric, noncollinear ferrielectric NC90, and ferroelectric phases. The numbers in parentheses in cyan circles are the numbers of the respective proton configurations from Table I. The hydrogen bond indices $f = 1, 2, 3, 4$ are shown. The green arrows indicate the polarization vectors $\mathbf{P}_\pm$ of the two sublattices. The red and cyan arrows show the proton flipping at the transitions from the configuration (3) to configurations (2), (4), and (1). The NC90(2), NC90(4), and FE phases are the FE-α (ii), FE-α (iv), and FE-β (iii) phases, respectively, in the notations of Ref. [5].

of which components $P_{1\pm}, P_{3\pm}$ are given by Eqs. (27), and the polarization vector $\mathbf{P}_+$ of the fully ordered plus sublattice, being determined from Eqs. (30) and (27) at $\eta_{f+} = 1$. It should be noted that the noncollinearity angle does not depend on the dipole moments $\mu^H + \mu^\pi_\parallel$ or $\mu^\pi_\perp$ explicitly.

It is expected that as long as $\mu^H + \mu^\pi_\parallel > \mu^\pi_\perp$, the positive external field E_1 switches the polarization in the minus sublattice only, whereas in the plus sublattice the polarization basically does not rotate. The situation is obviously reversed if $E_1 < 0$. The definition (29) of the noncollinearity angle θ is based on this assumption.

At zero temperature, the field-induced polarization rotation should occur via switching between the four lateral proton configurations (configurations 1–4 in Table I). Figure 5 illustrates the possible ground-state arrangements of protons in the two sublattices, under assumption that the plus sublattice polarization is not rotated. We also indicate which protons in the minus sublattice should be flipped along the respective hydrogen bond in order to switch to a different configuration. Flipping of the proton at the fth bond means a change of a sign of the respective order parameter η_{f-}. The values (signs) of the order parameters $\eta_{1\pm}$ and $\eta_{2\pm}$ in each phase are also given in the figure. Note that $\eta_{3\pm}$ and $\eta_{4\pm}$ are related to $\eta_{1\pm}$ and $\eta_{2\pm}$ via Eq. (16).

As one can see, the system ground-state configuration can be antiferroelectric ($\theta = 180^\circ$), ferroelectric ($\theta = 0$), and noncollinear ($\theta = 90^\circ$), with the minus sublattice polarization rotated by 90°. Horiuchi *et al.* [5] call the latter configuration the ferroelectric (FE)-α phase. Strictly speaking, it is not ferroelectric, but noncollinear ferrielectric, with perpendicular and distinct (by their magnitude at nonzero temperature) polarizations of the two sublattices. We shall denote it as NC90. The predicted [5] FE-β phase with parallel polarizations of the two sublattices is indeed collinear ferroelectric; it is simply FE in our notations.

There are two possible realizations of the NC90 phase: First, when the ground-state configuration for the minus sublattice is configuration 2, and second, when it is configuration 4. The minus sublattice polarization vectors of these two realizations are antiparallel to each other and perpendicular to the plus sublattice polarization. These two versions of the NC90 phase will be denoted as NC90(2) and NC90(4), respectively. The protons with $f = 2, 4$ are flipped at the transition from the AFE phase to the NC90(2) phase, and the protons with $f = 1, 3$ at the transition to the NC90(4) phase.

Note that Fig. 5 corresponds to the fully saturated system. When the temperature is raised, the directions of the polarization vectors and the values of the noncollinearity angle θ and of the order parameters $\eta_{f\pm}$ will deviate from those shown in the figure due to the thermal fluctuations.

C. The phase diagram

To construct the T-E_1 phase diagram of the squaric acid, we analyzed the temperature and field behavior of the quantities from Fig. 4. The temperature curves of these quantities at different fields can be found in the Appendix. No change of sign of η_{f+} was observed, which means that the plus sublattice polarization indeed is not switched by the field E_1.

The phase diagram, obtained with the adopted set of the model parameters, is shown in Fig. 6. We detected three lines of the first-order phase transitions I, II, and III. The lines I and II terminate at the critical points BCE$_1$ and BCE$_2$, which, as will be discussed later, are, in fact, bicritical end points [28]. The line III ends at the tricritical point TCP. The line of the second-order phase transitions IV starts at the tricritical pont TCP and terminates at the critical end point CEP, lying at the line of the first-order transitions I in a close vicinity of the bicritical end point BCE$_1$. The coordinates of the critical points, obtained with this set of the model parameters, are the

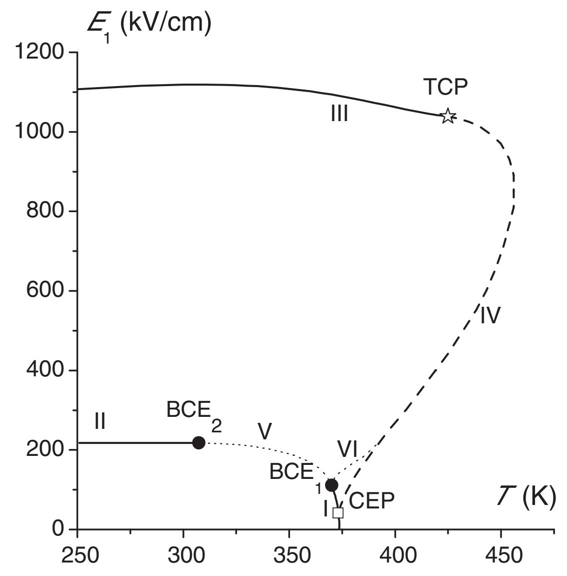

FIG. 6. The T-E_1 phase diagram of the squaric acid. Solid and dashed lines indicate the first- and second-order phase transitions, respectively. Dotted lines are the supercritical lines, corresponding to the loci of smeared maxima in the field curves of the dielectric permittivity. The open square, star, and full circles indicate the critical end point, tricritical point, and bicritical end points, respectively.

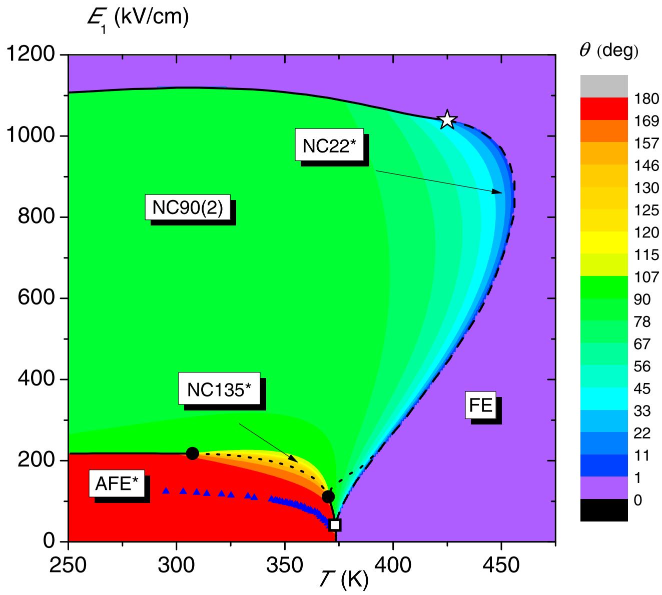

FIG. 7. The T-E_1 phase diagram of the squaric acid, overlapping the T-E_1 color contour plot of the noncollinearity angle θ. Black and white lines and symbols are the same as in Fig. 6. Blue full triangles ▲ are the experimental points [5].

following:

$$\begin{aligned}
\mathrm{BCE}_1 &: T_{\mathrm{bc1}} = 370\,\mathrm{K}, \quad E_{\mathrm{bc1}} = 111\,\mathrm{kV/cm},\\
\mathrm{BCE}_2 &: T_{\mathrm{bc2}} = 307\,\mathrm{K}, \quad E_{\mathrm{bc2}} = 217\,\mathrm{kV/cm},\\
\mathrm{TCP} &: T_{\mathrm{tcp}} = 425\,\mathrm{K}, \quad E_{\mathrm{tcp}} = 1039\,\mathrm{kV/cm},\\
\mathrm{CEP} &: T_{\mathrm{cep}} = 373\,\mathrm{K}, \quad E_{\mathrm{cep}} = 41\,\mathrm{kV/cm}.
\end{aligned}$$

In addition to the sharp anomalies at the first- and second-order phase transitions, the temperature curves (isofields) of the dielectric permittivity ε_{11} at different values of the field also exhibit several smeared anomalies (see, e.g., Figs. 13–16 in the Appendix), and so do the field curves (isotherms) of the permittivity at different temperatures. Loci of the anomalies in the permittivity isotherms are indicated in the phase diagram by the dotted lines V and VI. Line V connects BCE$_1$ and BCE$_2$, whereas line VI starts in a close vicinity of BCE$_1$ and terminates at line IV of the second-order transitions (see Fig. 10 in the Appendix for a closeup of this part of the phase diagram). Line V appears to be a continuation of the lines of the first-order transition lines I and II beyond the bicritical end points BCE$_1$ and BCE$_2$, and the parallels can be seen with the Widom lines, observed in ferroelectrics in electric fields applied along the axis of spontaneous polarization [7–9]. The origin of line VI is less clear. In more detail, the supercritical behavior of squaric acid will be explored elsewhere.

To identify the predicted phases, it is most efficient and informative to look at the phase diagram overlapped with the T-E_1 color gradient plot of the noncollinearity angle θ, as in Fig. 7.

The phase, existing at low temperatures and fields (the red region), is, strictly speaking, noncollinear (canted) antiferrielectric, as the true AFE phase with exactly antiparallel sublattice polarizations and zero net polarization exists at zero field or zero temperature only. However, at nonzero fields, only a slight rotation of the minus sublattice polarization takes place in this region, discernible mostly at its upper right boundary. This phase with $\theta \approx 180^\circ$ is very close to the initial AFE phase and will be denoted as AFE*.

The phase between the transition lines II, III, and IV (the green and blue regions in Fig. 7) is the noncollinear ferrielectric phase NC90. In this phase, the noncollinearity angle θ is mostly close to 90°, only rapidly decreasing to zero at increasing temperature within a narrow (blue) stripe along the second-order phase transition line IV. Within this stripe, which we shall denote as NC22*, a minor continuous rotation of the plus sublattice polarization takes place, and the order parameter η_{1-} becomes positive (see Figs. 12–19).

The value of the noncollinearity angle θ alone is not sufficient to distinguish between the two realizations of the NC90 phase. However, examining the temperature curves of the order parameters η_{f-} at crossing line II (see Figs. 14 and 15), one can see that it is the protons with $f = 2, 4$ that are flipped at this transition. Hence, the phase between the lines II and III is NC90(2), and the proton configuration 2 of the Table I is realized as the ground-state one at these fields E_1. Preliminary calculations show that for the diagonally directed field E_1-E_3 the phase diagram topology is the same, but the intermediate phase is NC90(4); that is, the proton configuration 4 is the ground-state one between lines II and III.

The phase, stabilized within the narrow wedge between lines I and IV with the tip at CEP, is noncollinear, with the temperature variation of the angle θ analogous to that in the NC90(2) phase. It is, however, possible that the phase in this wedge is different from NC90(2). In that case, line VI would signal the crossover from this phase to NC90(2). So far it is difficult to determine the criteria by which we could unambiguously distinguish between these two noncollinear phases. Hence, bearing this mentioned possibility in mind, we shall nonetheless take for now that within this wedge the phase NC90(2) is realized.

The phase observed at high fields and low temperatures and at high temperatures and any nonzero field (the purple region on the phase diagram) is the same collinear field-induced ferroelectric phase (FE) with $\theta = 0$. The true paraelectric phase with zero sublattice polarizations exists only at $E_1 = 0$. A transition from any noncollinear phase to the collinear FE phase can be realized only by crossing at least one line of the phase transitions of the first or second order. In this phase, the largest rotation of the plus sublattice polarization can be seen (Figs. 12–19).

The first-order transition lines I and II end at the critical points BCE_1 and BCE_2, around which the system can pass smoothly from one ordered phase, AFE*, to another ordered phase, NC90. Such critical points, terminating the lines of the first-order transitions between two ordered phases, are usually called bicritical end points [28], or, alternatively, double critical end points [29] or ordered critical points [30].

Within the region between the BCE_1 and BCE_2 points (orange to yellow in Fig. 7), the mentioned smooth crossover between the AFE* and NC90(2) phases occurs. Here the minus sublattice polarization rotates continuously with increasing field and becomes perpendicular to the plus sublattice polarization; thus the noncollinearity angle θ changes gradually from $\approx 180^\circ$ to $\approx 90^\circ$. We shall refer to this region as NC135*. The crossover line V goes through it.

Hence, the theory predicts that on increasing the field at temperatures below $T_{\mathrm{bc}2}$ the system undergoes two successive first-order phase transitions, associated with the polarization switching. One is accompanied by the change of θ from $\approx 180^\circ$ to $\approx 90^\circ$ (the minus sublattice polarization jumps by 90°), whereas at the other θ jumps from $\approx 90^\circ$ to 0° (the minus sublattice polarization jumps again by 90°, resulting in its total rotation by 180°, as compared to the initial AFE phase). By this, our theory corroborates the findings of Horiuchi *et al.* [5,14] about the first transition and expands them about the second one. Let us now compare our results and the previous ones [5,14] in more detail.

Depending on temperature, the low-field polarization switching occurs at the first-order transition line II, crossover line V, and then line I between the points BCE_1 and CEP; i.e., the switching is either a phase transition or a crossover. The temperature variation of the switching field is depicted in Fig. 8. It is well described by the power law $(T_{\mathrm{N}0} - T)^{1/\Phi}$ with different exponents: $\Phi \approx 2.7$ at $T_{\mathrm{N}0} - T$ between 0.4 and 7 K and $\Phi \approx 3.8$ at $T_{\mathrm{N}0} - T$ between 7 and 21 K. Qualitatively, the power law and the change of its exponent with temperature are in agreement with the experimental observations for the switching fields to the FE-α phase [5]. Quantitatively, the calculated switching fields are about twice as high as experimental ones, and the exponent in the power law 1/3.8 is smaller than experimental $\approx 1/3$.

As far as the second high-field transition from the NC90 to the FE phase is concerned, the earlier calculations [14] predicted that it could be induced by the electric fields applied along the diagonals in the ac plane: $E_1 \pm E_3$. The present model predicts such a transition for the field E_1 as well. Experimentally, the transition to the FE phase, induced by the electric field E_1 or $E_1 + E_3$, has not been detected so far, because of the dielectric breakdown of crystal samples at fields yet below 200 kV/cm [5,31].

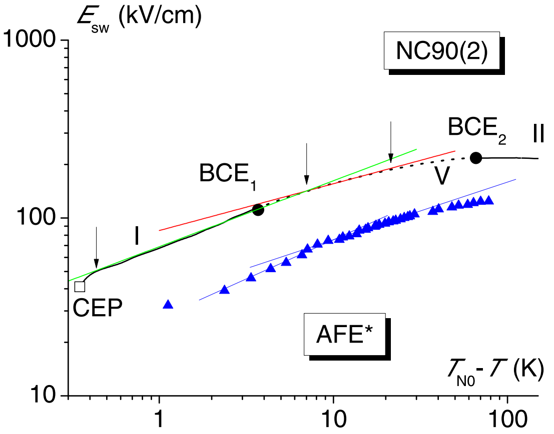

FIG. 8. The switching field as a function of temperature. The black and white lines and symbols are the same as in Fig. 6. The red line: $E_1 = 85(T_{\mathrm{N}0} - T)^{1/3.8}$; the green line: $E_1 = 69(T_{\mathrm{N}0} - T)^{1/2.7}$. The arrows indicate the temperature ranges, where these power laws fit the calculated $E_{sw}(T)$ curve. Blue triangles: experimental points of Ref. [5] for the transition to the FE-α phase; blue lines: linear (for the log scales) approximations of the experimental points.

The depolarization field, potentially arising at large values of the net polarization induced by high external electric fields, should further stabilize the NC90 phase. Hence, unless the crystal splits into domains, or a screening space-charge layer is formed at the crystal surfaces, the values of the external field required to reach the NC90-FE transition can be even less likely to be below the dielectric strength of a real crystal. The shape and size of the samples are also important. Theoretical modeling of these phenomena, however, lies beyond the scope of the present study.

As already mentioned, the adopted set of the values of the model parameters ν_0', $\mu^H + \mu_\parallel^\pi$, and $\mu_\perp^\pi$ is not unique. The choice of these values was dictated by the fit to the experimental [5] temperature curves of the permittivity ε_{11} and switching field E_{sw} they provided, as illustrated in Figs. 4 and 8. Nonetheless, the values of these parameters still can be varied within certain limits, and other acceptable sets of them can be found, which provide similar agreement with the experiment.

The calculated position of the transition line III is most sensitive to the values of these parameters. For different acceptable sets, the corresponding to the line III fields may vary at least between 600 and 1200 kV/cm and possibly in a wider range. In view of this uncertainty, line III should be considered only as a qualitative theoretical prediction of the very existence of such a transition induced by the field E_1, rather than a quantitative estimate of the transition fields.

Generally speaking, the very topology of the T-E_1 phase diagram can change when the model parameters are changed significantly. For the mentioned acceptable sets, the phase diagram topology mostly remains as shown in Fig. 7. However, for some of such sets, particularly for those with lower

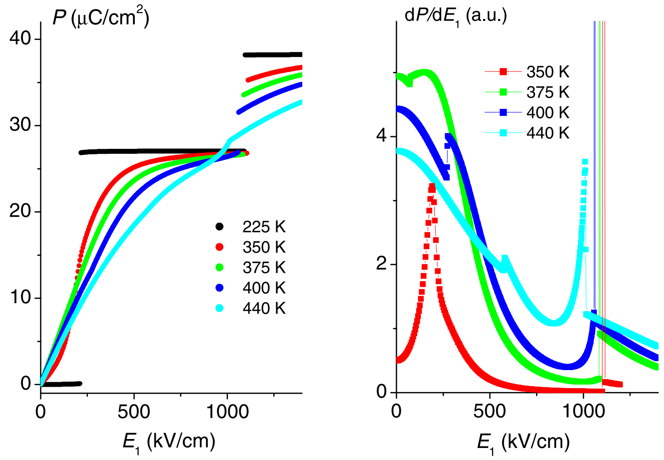

FIG. 9. The calculated field dependences of total polarization P (left) and its field derivative dP/dE_1 (right) of the squaric acid at different temperatures: 225 K ($T < T_{\rm bc2}$), 350 K ($T_{\rm bc2} < T < T_{\rm bc1}$), 375 K ($T_{\rm cep} < T < 390\,{\rm K}$), 400 K (390 K $< T < T_{\rm tcp}$), and 440 K ($T_{\rm tcp} < T < 455\,{\rm K}$). The values of dP/dE_1 for 350 K are divided by 4.

values of ν_0', the tricritical point (TCP) between lines III and IV can split into a system of a bicritical end point and a critical end point, lying on the line III. In this case a noncollinear phase, different from NC90, is stabilized in the newly emerged wedge between lines III and IV. Such a splitting is a well-known phenomenon in the theory of metamagnetic transitions, occurring, for instance, in the two-sublattice Ising model at different ratios between competing intrasublattice and intersublattice interactions [28]. There are indications that for this and similar models, the splitting is an artifact of the used MFA (see, e.g., Refs. [32] and references therein). It is therefore possible that although our model is more complicated than the mentioned Ising model, the other predicted by the present calculations split system of critical points, CEP-BCE$_1$, may also be an artifact of the MFA used for the long-range interactions. Further theoretical studies, e.g., Monte Carlo calculations, may shed some light on this problem. The presence of this splitting should be visible in the temperature curves of the permittivity (see Fig. 12) and specific heat. Thus, their experimental measurements with the bias field E_1 in the range 30–150 kV/cm might help to establish the details of the phase diagram and to ascertain the values of the model parameters by providing additional data for the fitting procedure.

D. Polarization

Some characteristic (but not all possible) types of the field dependences of the total crystal net polarization P at different temperatures are illustrated in Fig. 9. At low temperatures, $T < T_{\rm bc2}$, the system undergoes two first-order phase transitions with jumps of polarization, when lines II and III are crossed. Three polarization plateaus are observed: zero AFE net polarization below the first transition, intermediate ferrielectric between the transitions, and ferroelectric above the second transition. The theoretical values of polarization in the fully ordered NC90(2) and FE phases are about 1.5 times higher than the predicted by the Berry phase calculations 16.4 and 23.2 $\mu{\rm C/cm}^2$ [5].

At higher temperatures, the polarization plateaus are smeared out. At $T_{\rm bc2} < T < T_{\rm bc1}$, the lower jump of the polarization is replaced with a steep gradual increase, as the field increases across the region NC135* of the phase diagram, while the upper jump of the polarization persists. A high rounded peak of dP/dE_1 corresponds to this steep increase; the loci of such peaks in this temperature range correlate with the crossover line V.

At $T_{\rm cep} < T < T_{\rm tcp}$, the system undergoes the second-order phase transition at line IV and the first-order transition at line III. At the lower transition, only a small, practically invisible kink in the field dependence of polarization takes place. The anomaly, however, is easily detected in the field derivative of polarization. At $T_{\rm cep} < T \lesssim 390\,{\rm K}$, this anomaly is followed by a shallow maximum of dP/dE_1. Loci of these maxima correlate with the crossover line VI.

At $T_{\rm tcp} < T < 455\,{\rm K}$, a reentrant behavior is observed, as the system crosses line IV twice. Two kinks of the $P(E_1)$ take place, with the lower anomaly again being identifiable only in the field derivative of polarization. Above 455 K, the system undergoes no phase transition and the field dependence of polarization is smooth (not shown in the figure).

Detailed illustration of the temperature behavior of the order parameters, noncollinearity angle, permittivity, and lattice strains at different values of the electric field E_1 can be found in the Appendix.

IV. CONCLUDING REMARKS

We have presented the modification of the deformable two-sublattice proton ordering model [19], aimed to describe the effects of the external electric fields applied to antiferroelectric crystals of squaric acid. The dipole moments associated directly with protons and with the π bonds that can be switched by proton rearrangement are included into the model.

The major predicted effect of the positive electric field E_1 is a switching or continuous rotation of polarization in the minus sublattice. The system state is best described by the introduced noncollinearity angle θ, which is the angle between the polarization vectors of the plus and minus sublattices, Eq. (29).

The constructed T-E_1 phase diagram consists of the nearly antiferroelectric (in fact, slightly noncollinear antiferrielectric) phase with almost antiparallel sublattice polarizations (AFE*, $\theta \approx 180^\circ$), noncollinear phase with nearly perpendicular sublattice polarizations (NC90, $\theta \approx 90^\circ$), and collinear ferroelectric phase (FE, $\theta = 0$). More specifically, flipping of protons at the $f = 2, 4$ bonds in the minus sublattice at the transition between the AFE* and NC90 phases takes place, which means that the NC90(2) version is realized (see Fig. 5). The crossover region NC135* is also present in the diagram, where the noncollinearity angle θ changes gradually from about 180° to about 90° due to rotation of the minus sublattice polarization, and the crossover between the AFE* and NC90(2) phases occurs.

The continuous rotation of the sublattice polarization is a statistically averaged phenomenon. The dipole moment of each $H_2C_4O_4$ group can only be oriented along the specific directions, described in Table I. At zero temperature, when $|\eta_{f\pm}| = 1$, all the protons of a sublattice are in the same lateral configuration (one of the configurations 1–4 of Table I). Hence, the total sublattice polarization can only be directed along one of the four directions, as shown in Fig. 5. However, at higher temperatures, due to the interplay of the switching external field and thermal fluctuations, protons around some of the C_4O_4 groups can rearrange into other configurations, including the single-ionized ones (configurations 7–14 of Table I), thereby switching the dipole moments of these groups. Because of this disorder, the resulting vector of the total sublattice polarization can be directed arbitrarily, as determined by relative populations of different proton configurations.

The predicted low-temperature sequence of the phase transitions AFE*→ NC90 → FE is the result of the interplay of two mechanisms: external electric field, trying to realign the minus sublattice polarization, and the antiferroelectric long-range interlayer interactions between protons, trying to stabilize the antiparallel orientation of the sublattice polarizations. Because of the unique geometry of the hydrogen bonds in squaric acid, the polarization switching is a two-step process. When the field is large enough to partially overcome the AFE correlations, the minus sublattice polarization first rotates by 90°. Only when the field is sufficiently increased, then the AFE correlations are completely overcome, and the collinear ferroelectric state is induced.

The theoretical results qualitatively agree with the experimental findings [5] for the transition or crossover between the AFE* and NC90 phases. The calculated values of the net polarization and the switching fields, however, are perceptibly higher than observed experimentally. The agreement with experiment, at least for the switching fields, could possibly be improved by inclusion of nonlinear terms into the system Hamiltonian. It would also be very interesting to explore in detail the nature of the supercritical lines found in the temperature-electric field phase diagram as well as to consider the effects induced by electric fields with orientations different from E_1. Such calculations are currently under way, and the results will be published elsewhere.

APPENDIX

Here we shall use the notations for the phase transition lines from Fig. 6 and for the phases from Fig. 7. The transition lines, the supercritical lines obtained from the permittivity isotherms, and critical end points for the lower part of the T-E_1 phase diagram are replotted in Fig. 10. In this figure, we also indicated the loci of the smeared anomalies in the temperature curves of the dielectric permittivity (lines VII and VIII). In more detail, these anomalies are discussed below.

It is also convenient to introduce the angles of rotation of the plus and minus sublattice polarizations

$$\theta_\pm = \arccos \frac{\eta_{1\pm} + \eta_{2\pm}}{\sqrt{2\left(\eta_{1\pm}^2 + \eta_{2\pm}^2\right)}},$$

which are the angles between the actual plus and minus sublattice polarization vectors $\mathbf{P}_\pm$, Eq. (30), and the polarization vector $\mathbf{P}_+$ of the fully ordered plus sublattice, determined from Eqs. (30) and (27) at $\eta_{f+} = 1$. Obviously, for the noncollinearity angle, we have $\theta = |\theta_+ - \theta_-|$. We shall plot the temperature curves for the angles θ_+ and θ only.

When the electric field E_1 is increased until up to $E_{\rm cep}$ (Fig. 11), the system behavior remains basically the same as at zero field, except for appearance of small field-induced positive values of $\eta_{f\pm}$ above the transition. A perceptible rotation of the plus sublattice polarization is seen only above the transition in the FE phase, as follows from the temperature curve of the angle θ_+.

Qualitative changes occur when the field is raised above $E_{\rm cep}$ (see Fig. 12). At fields between $E_{\rm cep}$ and $E_{\rm bc1}$, the system undergoes two successive phase transitions of the first and then second orders at lines I and IV on increasing temperature. The permittivity, which has an upward jump at the only phase transition at fields below $E_{\rm cep}$ (see Fig. 11), now exhibits a high sharp peak at approaching the first-order transition and a finite downward jump at the second-order transition.

Between the transitions, the noncollinearity angle θ rapidly decreases from above 90° down to zero. A perceptible rotation of the plus sublattice polarization is observed only in the NC22* region, at approaching the second transition, and in the FE phase. On the other hand, the order parameter η_{2-} changes sign at the first-order transition, indicating a jump-like switching of the minus sublattice polarization. At further increase of the field, the jumps of the pseudospin mean values at the line I decrease, until at $E_{\rm bc1}$ this transition becomes of the second order: The bicritical end point BCE_1 is reached.

At fields above $E_{\rm bc1}$, the system undergoes only the second-order transition at line IV (see Fig. 13). Below the transition, the system goes through the crossover region NC135*, where the permittivity has a maximum at line VII and a smeared kink at a higher temperature, whereas the order parameter η_{2-} rapidly but continuously increases to positive values. The

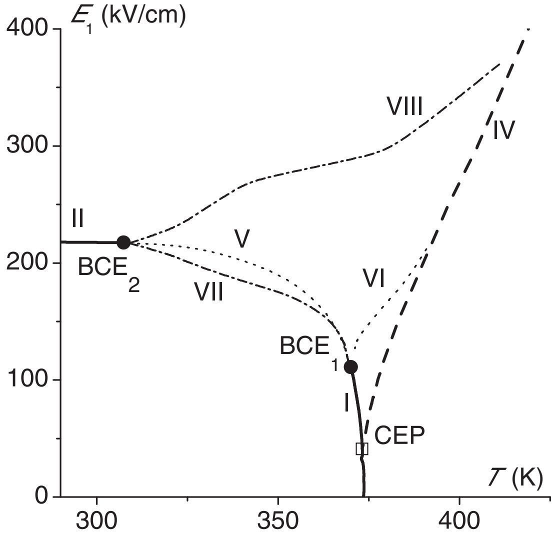

FIG. 10. The low-field closeup of the T-E_1 phase diagram. The solid, dashed, and dotted lines (phase transition lines I, II, and IV, and supercritical lines V and VI) and symbols (the critical end points BCE_1, BCE_2, and CEP) are the same as in Fig. 6. The dash-dotted lines VII and VIII are the loci of the smeared maxima in the permittivity isofields.

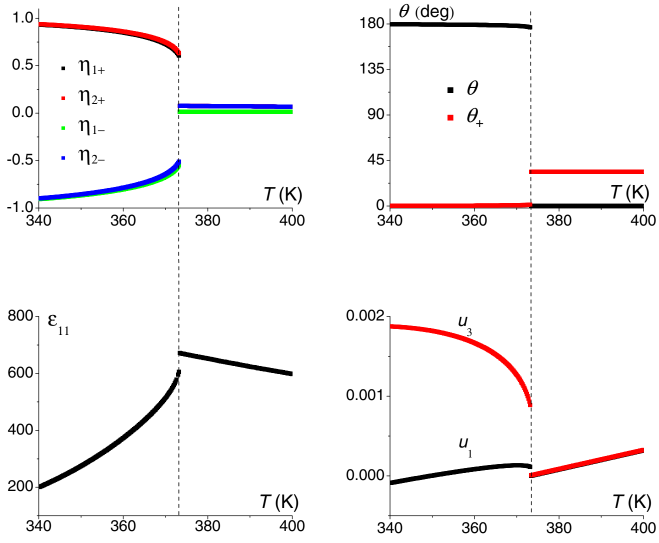

FIG. 11. The calculated temperature dependences of the order parameters $\eta_{f\pm}$ (upper left), the noncollinearity angle θ and angle of rotation of the plus sublattice polarization θ_+ (upper right), dielectric permittivity (lower left), and lattice strains u_1 and u_3 (lower right) of squaric acid at $E_1 = 35$ kV/cm. Vertical dashed lines are drawn through the phase transition points.

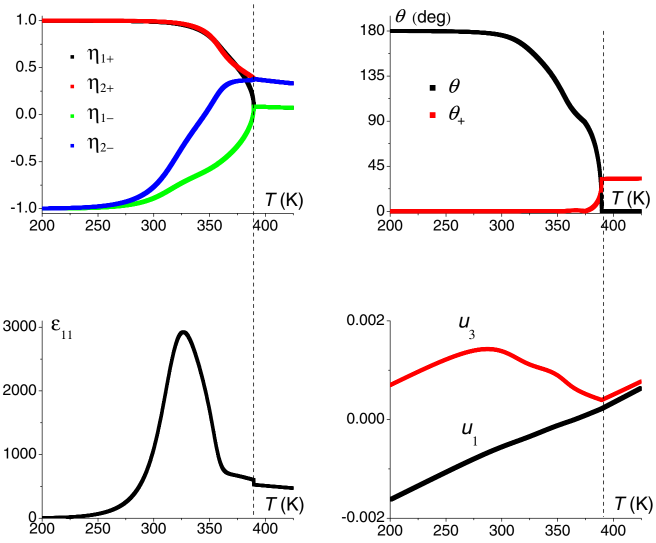

FIG. 13. Same as in Fig. 11 at $E_1 = 200$ kV/cm.

smooth change of the order parameter η_{2-} sign means the gradual rotation of the minus sublattice polarization and a decrease of the noncollinearity angle θ from about 180° to about 90°. The sharp peaks of the dielectric permittivity and jumps of the order parameters $\eta_{f\pm}$ at the transition at the line I, observed at fields below $E_{\mathrm{bc}1}$ (Fig. 12), transform into inflections in the temperature curves of η_{f-} and θ and into the rounded peak at the line VII. The closer is the field to the bicritical end point BCE$_2$, the sharper and higher this rounded peak becomes.

In a narrow field range just below $E_{\mathrm{bc}2}$, the system can cross the line II (see Fig. 14), where it undergoes the first-order transition from the AFE* to NC90 phase with decreasing temperature. The transition is accompanied by a δ-like peak of the permittivity. Also the noncollinearity angle θ jumps from 180° to 90°, and η_{2-} abruptly changes its sign. It means that at low temperatures configuration 2 becomes the ground-state one in the minus sublattice, and the NC90(2) version of the noncollinear phase is realized above line II.

The strains u_1 and u_3 do not exhibit any anomaly at crossing line II at low temperatures. This follows from Eqs. (25), as the fitting parameters ψ_i' were arbitrarily set equal to ψ_i. As one can see, the jumps of the strains at the transition, when only the sign of one order parameter, in this case η_{2-}, is changed, are governed by the magnitudes of the differences $(\psi_i - \psi_i')$. Experimental measurements of the lattice constants behavior at the field-induced transition at line II would provide the data necessary to determine the values of ψ_i'.

At higher temperatures, the system goes through the crossover region NC135*, where the permittivity has a

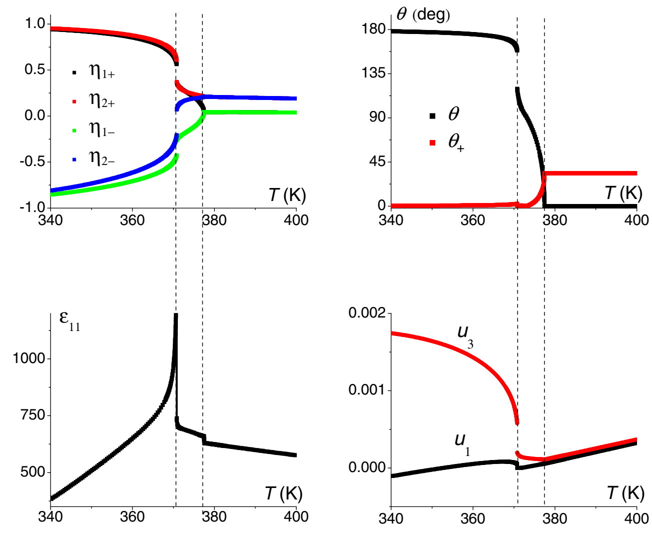

FIG. 12. Same as in Fig. 11 at $E_1 = 100$ kV/cm.

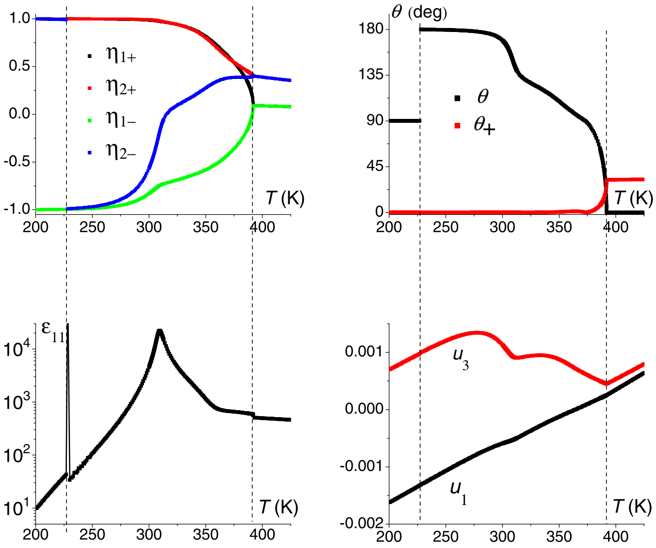

FIG. 14. Same as in Fig. 11 at $E_1 = 216$ kV/cm.

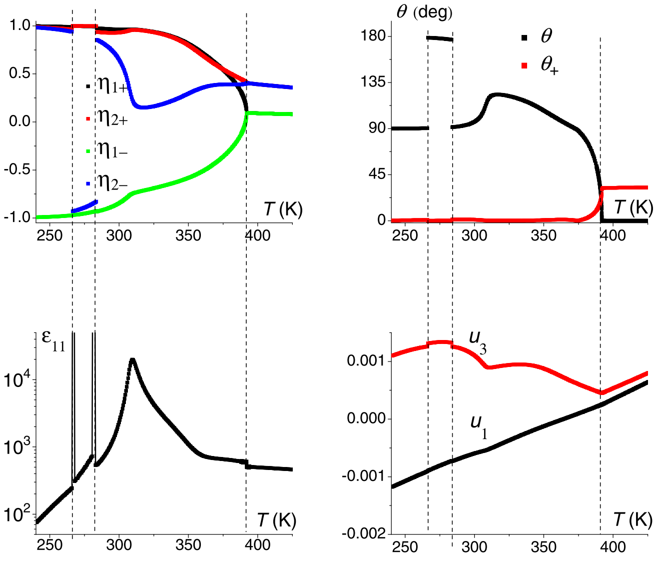

FIG. 15. Same as in Fig. 11 at $E_1 = 217.7$ kV/cm.

rounded high peak at line VII and a kink at a higher temperature, and then undergoes the second-order phase transition at line IV with the downward jump of the permittivity. A minor rotation of the plus sublattice polarization is observed at temperatures just below the transition, in the NC22* region, and above it, in the FE phase.

The line II is weakly nonmonotonic. Above E_{bc2}, there exists a very narrow range of the field E_1, where at increasing temperature the system can exhibit a reentrant behavior from the NC90(2) to AFE* and back to the NC90(2) phase at low temperatures. This reentrant behavior, as illustrated in Fig. 15, results in two jumps of order parameter η_{2-} and of angle θ, δ-like peaks of the dielectric permittivity, and barely visible discontinuities of the strain u_3. At temperatures above these transitions, the permittivity behavior is the same as at lower fields (see Fig. 14), only that the smeared maximum corresponds to the line VIII now, where the system enters the crossover region NC135* from the NC90(2) phase.

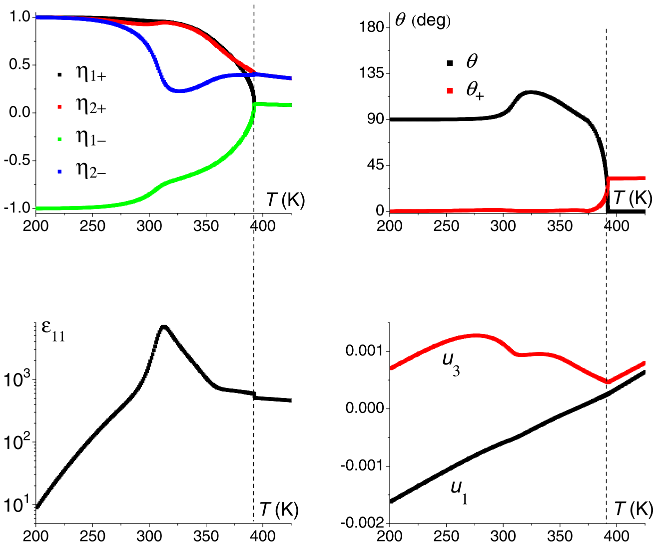

FIG. 16. Same as in Fig. 11 at $E_1 = 220$ kV/cm.

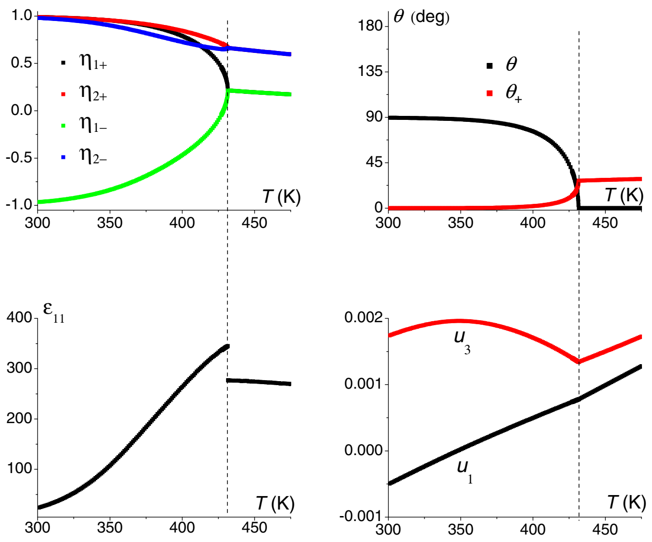

FIG. 17. Same as in Fig. 11 at $E_1 = 500$ kV/cm.

In the field range above line II and below about 250 kV/cm, the system behavior, illustrated in Fig. 16, is the same as at lower fields, shown in Fig. 15, except for the absence of two first-order transitions at line II.

As the field E_1 is increased, the kink in the temperature curve of the permittivity disappears, and only the rounded peak at line VIII and the jump at the second-order phase transition at line IV remain. The peak temperature increases with the field, following line VIII, until at around 375 kV/cm it merges with the second-order phase transition at line IV and disappears (see Fig. 10). Above that and up to the field of the tricritical point E_{tcp}, the temperature curves of the permittivity exhibit only the anomaly at the line IV, as shown in Fig. 17. The permittivity monotonically increases with temperature below the transition and has a downward jump at the transition. The jump magnitude first decreases with increasing field, but at about 850 kV/cm starts to increase again, until the finite peak transforms into a δ-like one at the tricritical point TCP.

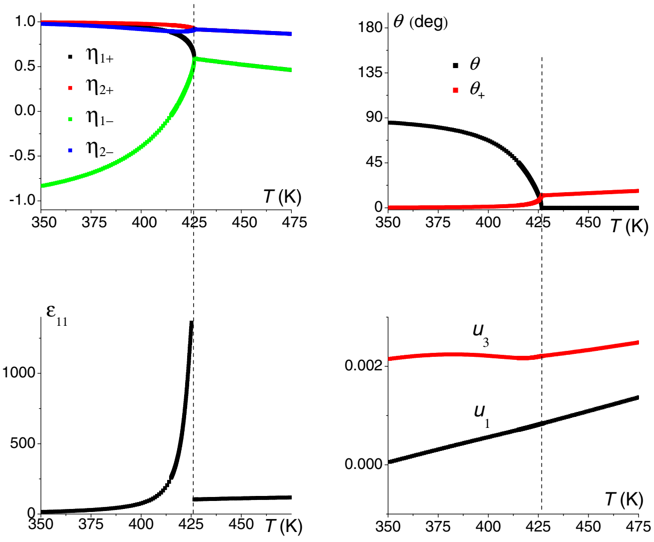

FIG. 18. Same as in Fig. 11 at $E_1 = 1038$ kV/cm.

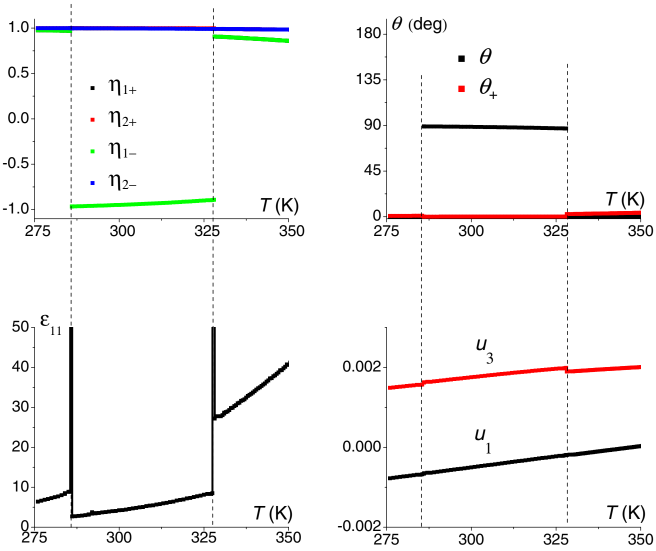

FIG. 19. Same as in Fig. 11 at $E_1 = 1045$ kV/cm.

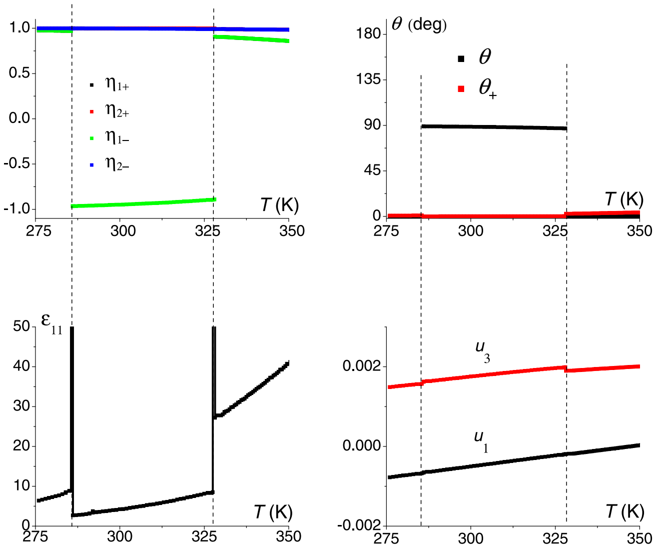

FIG. 20. Same as in Fig. 11 at $E_1 = 1116$ kV/cm.

No additional smeared maximum in the temperature curves of the permittivity is observed in the vicinity of the TCP (Fig. 18). Such maxima, however, are expected to be detected in the temperature curves of dP_1/dT [33]. At the tricritical point, line IV terminates, and at higher fields the phase transition, now at line III, is of the first order, as seen in Fig. 19.

The line III is nonmonotonic, just like line II. Therefore, at higher fields the system exhibits a reentrant behavior between the nearly fully ordered FE and NC90(2) phases, undergoing two first-order phase transitions at line III, as shown in Fig. 20. The permittivity has δ-like peaks at these transitions, and the order parameter η_{1-} drops from $\approx$1 to ≈ -1 and jumps back to $\approx$1, at which the noncollinearity angle changes from zero to 90° and back to zero. When increasing the field, these transitions move closer and merge at about 1120 kV/cm. Above that field, the system is in the FE phase at all temperatures.

The general conclusions that can be drawn about the presented temperature dependences of the order parameters and strains are the following:

(1) When crossing line II, the order parameter η_{2-} of the minus sublattice changes its sign, indicating flipping of protons at $f = 2, 4$ bonds and the transition to the NC90(2) phase (see Fig. 5). On the other hand, the order parameters η_{f+} of the plus sublattice never change their sign under the positive electric field E_1. A perceptible but still small rotation of the plus sublattice polarization, described by the angle θ_+, is observed at high temperatures only, in the NC22* region and in the FE phase.

(2) The strains u_3 and u_1 exhibit discernible discontinuities at those phase transitions, when the absolute values of the order parameters $\eta_{f\pm}$ are changed significantly. At the transitions, when only a sign of η_{f-} is changed, these strains remain unaffected. The strain u_2, describing the crystal deformation in the direction perpendicular to the polarization sheets, was equally found to be unaffected by the field E_1. These results disagree with the earlier calculations [14], predicting that the jumps of all three lattice constants are to be observed at the field-induced phase transitions associated with the sublattice polarization rotation and that in the field E_1 the largest discontinuity is exhibited by the strain u_1. The disagreement could be possibly removed by choosing different values for the parameters ψ_i and ψ_i'. Experimental data for the lattice constants behavior at the field-induced transition at line II would also help to determine the values of the fitting parameters ψ_i'.

(3) It should be remembered that the graphs in the Appendix illustrate the types of the system temperature behavior, obtained for the adopted set of the model parameters. If the values of the parameters are changed, the presented curves may change quantitatively, or become irrelevant, or even entirely different types of them may emerge.

[1] D. Semmingsen, Z. Tun, R. J. Nelmes, R. K. McMullan, and T. F. Koetzle, On the temperature dependence of the hydrogen bond order in squaric acid: Neutron diffraction studies at four different temperatures, Z. Kristallogr. **210**, 934 (1995).

[2] D. Semmingsen, F. J. Hollander, and T. F. Koetzle, A neutron diffraction study of squaric acid (3,4-dihydroxy-3-cyclobutene-1,2-dione), J. Chem. Phys. **66**, 4405 (1977).

[3] F. J. Hollander, D. Semmingsen, and T. F. Koetzle, The molecular and crystal structure of squaric acid (3,4-dihydroxy-3-cyclobutene-1,2-dione) at 121°: A neutron diffraction study, J. Chem. Phys. **67**, 4825 (1977).

[4] Y. Moritomo, Y. Tokura, H. Takahashi, and N. Mōri, Quantum Paraelectricity and Subsequent Disappearance of Bond Alternation of Molecule Caused by Proton Dynamics in Squaric Acid Crystal, Phys. Rev. Lett. **67**, 2041 (1991).

[5] S. Horiuchi, R. Kumai, and S. Ishibashi, Strong polarization switching with low-energy loss in hydrogen-bonded organic antiferroelectrics, Chem. Sci. **9**, 425 (2018).

[6] I. V. Stasyuk, R. R. Levitskii, A. P. Moina, and B. M. Lisnii, Longitudinal field influence on phase transition and physical properties of the KH_2PO_4 family ferroelectrics, Ferroelectrics **254**, 213 (2001).

[7] Z. Kutnjak, R. Blinc, and Y. Ishibashi, Electric field induced critical points and polarization rotations in relaxor ferroelectrics, Phys. Rev. B **76**, 104102 (2007).

[8] N. Novak, Z. Kutnjak, and R. Pirc, High-resolution electrocaloric and heat capacity measurements in barium titanate, EPL **103**, 47001 (2013).

[9] W. Ma, Polarization rotation associated critical phenomena in epitaxial $PbTiO_3$ thin films near room temperature, AIP Adv. **6**, 045310 (2016).

[10] T. Okada, Phenomenological theory of antiferroelectric transition. III. Phase diagram and bias effects of first-order transition, J. Phys. Soc. Jpn. **37**, 1226 (1974).

[11] I. Suzuki and Y. Ishibashi, Electric-field induced tricritical points in antiferroelectric phase transitions, J. Phys. Soc. Jpn. **52**, 187 (1983).

[12] I. Suzuki and Y. Ishibashi, Multicritical points in the applied field vs temperature phase diagrams of antiferroelectric transitions, J. Phys. Soc. Jpn. **52**, 2088 (1983).

[13] P. Tolèdano and M. Guennou, Theory of antiferroelectric phase transitions, Phys. Rev. B **94**, 014107 (2016).

[14] S. Ishibashi, S. Horiuchi, and R. Kumai, Computational findings of metastable ferroelectric phases of squaric acid, Phys. Rev. B **97**, 184102 (2018).

[15] E. Matsushita and T. Matsubara, Theory of phase transition in squaric acid, Progr. Theor. Phys. **64**, 1176 (1980).

[16] E. Matsushita and T. Matsubara, Theory of ferroelastic phase transition in squaric acid, Ferroelectrics **39**, 1095 (1981).

[17] E. Matsushita and T. Matsubara, Cluster theory of phase transition in squaric acid. I: Formulation and general discussion, Progr. Theor. Phys. **68**, 1811 (1982).

[18] B. K. Chaudhuri, P. K. Dey, and T. Matsuo, Phase transitions of quasi-two-dimensional antiferroelectric squaric acid ($H_2C_4O_4$) and ($D_2C_4O_4$) investigated by the Green's function technique, Phys. Rev. B **41**, 2479 (1990).

[19] A. P. Moina, Effects of diagonal strains and H-bond geometry in antiferroelectric squaric acid crystals, Condens. Matter Phys. **23**, 33704 (2020).

[20] D. Semmingsen and J. Feder, A structural phase transition in squaric acid, Solid State Commun. **15**, 1369 (1974).

[21] J. F. Nye, *Physical Properties of Crystals: Their Representation by Tensors and Matrices* (Clarendon Press, Oxford, UK, 1985).

[22] R. Blinc and S. Svetina, Cluster approximations for order-disorder-type hydrogen-bonded ferroelectrics. II. Application to KH_2PO_4, Phys. Rev. **147**, 430 (1966).

[23] R. R. Levitskii and B. M. Lisnii, Theory of related to shear strain u_6 physical properties of ferroelectrics and antiferroelectrics of the KH_2PO_4 family, Phys. Stat. Sol. (B) **241**, 1350 (2004).

[24] I. V. Stasyuk, R. R. Levitskii, and A. P. Moina, External pressure influence on ferroelectrics and antiferroelectrics of the KH_2PO_4 family: A unified model, Phys. Rev. B **59**, 8530 (1999).

[25] R. R. Levitskii, I. R. Zachek, T. M. Verkholyak, and A. P. Moina, Dielectric, piezoelectric, and elastic properties of the Rochelle salt $NaKC_4H_4O_6 \cdot 4H_2O$: A theory, Phys. Rev. B **67**, 174112 (2003).

[26] A. N. Klymachyov and N. S. Dalal, Magic angle spinning NMR on single crystals as a new aid in characterizing phase transitions: Application to squaric acid, Z. Phys. B Condensed Matter **104**, 651 (1997).

[27] K. H. Ehses, The thermal expansion of squaric acid, Ferroelectrics **108**, 277 (1990).

[28] J. M. Kincaid and E. G. D. Cohen, Phase diagrams of liquid helium mixtures and metamagnets: Experiment and mean field theory, Phys. Rep. C **22**, 57 (1975).

[29] C. S. O. Yokoi, M. D. Coutinho-Filho, and S. R. Salinas, Ising model with competing axial interactions in the presence of a field: A mean-field treatment, Phys. Rev. B **24**, 4047 (1981).

[30] M. Kaufman, P. E. Klunzinger, and A. Khurana, Multicritical points in an Ising random-field model, Phys. Rev. B **34**, 4766 (1986).

[31] S. Horiuchi (private communication).

[32] J. A. Plascak and D. P. Landau, Universality and double critical end points, Phys. Rev. E **67**, 015103(R) (2003).

[33] W. Selke, Anomalies in Ising metamagnets, Z. Phys. B **101**, 145 (1996).